RSC Advances

PAPER

View Article Online
View Journal | View Issue

Cite this: *RSC Adv.*, 2018, **8**, 22823

Global diabatic potential energy surfaces for the BeH_2^+ system and dynamics studies on the $Be^+(^2P)$ + $H_2(X^1\Sigma_g^+)$ → $BeH^+(X^1\Sigma^+)$ + $H(^2S)$ reaction

Zijiang Yang, Jiuchuang Yuan, Shufen Wang and Maodu Chen *

Received 21st May 2018
Accepted 14th June 2018

DOI: 10.1039/c8ra04305a

rsc.li/rsc-advances

The $Be^+(^2P)$ + $H_2(X^1\Sigma_g^+)$ → $BeH^+(X^1\Sigma^+)$ + $H(^2S)$ reaction has great significance for studying diabatic processes and ultracold chemistry. The first global diabatic potential energy surfaces (PESs) which are correlated with the lowest two adiabatic states $1^2A'$ and $2^2A'$ of the BeH_2^+ system are constructed by using the neural network method. *Ab initio* energy points are calculated using the multi-reference configuration interaction method with the Davidson correction and AVQZ basis set. The diabatic energies are obtained from the transformation of *ab initio* data based on the dipole moment operators. The topographical characteristics of the diabatic PESs are described in detail, and the positions of crossing between the V_{11}^d and V_{22}^d are pinpointed. On new diabatic PESs, the time-dependent quantum wave packet method is carried out to study the mechanism of the title reaction. The results of dynamics calculations indicate the reaction has no threshold and the product BeH^+ is excited to high vibrational states easily. In addition, the product BeH^+ tends to backward scattering at most collision energies.

1 Introduction

In recent decades, the interactions between metal ions and dihydrogen have received considerable attention due to their central roles in chemical reactions at low temperatures,[1–4] in hydrogen storage[5–8] and in astrophysics[9,10] among other fields. For the MH_2^+ (M = metal atoms) system, there are substantial experimental and theoretical studies concentrated on the spectroscopic properties of the M^+–H_2 complexes, which have been summarized in a review.[11] On the other hand, the reactive collisions between metal ions and molecular hydrogen (M^+ + H_2) are important objects to study reaction dynamics, and a broad range of M^+ ions have been performed by the guide ion beam methods in combination with theoretical calculations.[12–15]

The BeH_2^+ system has been widely studied in the related fields of cold and ultracold chemistry. In 2006, Roth *et al.*[2] studied the $Be^+(^2P)$ + H_2 → BeH^+ + H reaction by a laser-cooling ion trap apparatus with the millikelvin level translational temperatures of Be^+ ions. They measured the rate constant as high as 10^{-9} cm^3 s^{-1}, implying a barrierless reaction pathway. Sawyer *et al.*[16] applied the rotational-state-insensitive dissociation scheme to study photodissociation of BeH^+ molecular ions, which were generated by the reaction between laser-cooling Be^+ ions and H_2. The technique used in this experiment can take away a key limitation for large-scale quantum-information experiments. Moreover, Be^+ ions were widely used to sympathetically cool other atomic and molecular ions.[17–20] Those experiments may open new approaches for the studies about the coherent manipulation of quantum states and reactions relevant to interstellar molecules.

In contrast, the dynamics calculations for the title reaction have not been carried out. To study the reaction dynamics, the prerequisite is to establish an accurate potential energy surface (PES), which governs the nuclear dynamics. The first PES of the BeH_2^+ system using self-consistent-field and valence bond configuration interaction methods was reported by Poshusta *et al.*[21] The calculated energies of BeH_2^+ molecular ions were only in C_{2v} geometries. In 1983, Raimondi and Gerratt[22] used the spin-coupled valence bond theory to structure the ground state and several excited states adiabatic PESs for the Be^+ + H_2 reaction. The results showed that reaction for the ground state is endothermic by 1.57 eV, therefore Be^+ ions must be excited to produce BeH^+ molecular ions at a low collision energy. Artiukhin *et al.*[23] constructed a ground state adiabatic PES to investigate the structural and spectroscopic properties of the Be^+–H_2 complexes, the energy points were calculated at the CCSD(T) level. On this PES, the authors identified the T-shape Be^+–H_2 complex is the minimum energy structure.

For the title reaction, the reactants $Be^+(^2P)$ + $H_2(X^1\Sigma_g^+)$ and the products $BeH^+(X^1\Sigma^+)$ + $H(^2S)$ involve the lowest two adiabatic states ($2^2A'$ and $1^2A'$). Namely, the reaction starts from the lowest excited state and then intersects the ground state to enter into the product channel. Therefore, to study the reaction of electronically excited Be^+ ion with H_2 on diabatic PESs is required. In the diabatic representation, the Born–

Key Laboratory of Materials Modification by Laser, Electron, and Ion Beams (Ministry of Education), School of Physics, Dalian University of Technology, Dalian 116024, P. R. China. E-mail: mdchen@dlut.edu.cn

Oppenheimer approximation breaks down, and the conical intersection appears to connect the two states. As we know, there are no global diabatic PESs which are suited for dynamics studies of the $Be^+(^2P) + H_2(X^1\Sigma_g^+) \rightarrow BeH^+(X^1\Sigma^+) + H(^2S)$ reaction up to now. Due to the reaction can occur at very low temperatures, thus the accuracy of dynamics results is especially sensitive to the PES, and the long-range potentials are also very crucial within the low collision energy range. To achieve these requirements above, a mass of high-level *ab initio* energy points in a large configuration space are calculated and utilized to generate the diabatic energies by a proper diabatization method in this work. The neural network (NN) method is applied to construct the accurate global diabatic PESs for the two states ($2^2A'$ and $1^2A'$) of the BeH_2^+ system. Then, based on the diabatic PESs, the dynamics calculations of the title reaction are implemented using the time-dependent wave packet (TDWP) method.

2 Potential energy surfaces

2.1 Diabatization method

Direct access to the diabatic states of the electronic Hamiltonian would lead to considerable difficulties, so the acquisition of diabatic energies is usually based on the transformation of adiabatic data. The approaches of diabatic transformation can be divided two categories: the derivative-based methods and the molecular property-based methods. The derivative-based methods are the most rigorous approaches for studying diabatic effect, and have been applied to construct some molecular system diabatic PESs.[24–27] However, the calculation burden is too heavy to obtain the derivative couplings over a large coordinate space. Making use of suitable molecular properties to characterize the diabatic transformation is also effective methods, which have less computational effect compared to the derivative-based methods. Dipole moment,[28–32] angular momentum[33–35] and quadrupole moment[36] operators have been used to obtain the diabatic energies. The molecular property-based methods are adopted in this work, and a brief description about the diabatization scheme is presented. Considering the coupling of two states, the diabatic wave functions ϕ_i^d are constructed by a representation transformation from the adiabatic wave functions ψ_i^a

$$\begin{pmatrix} \phi_1^d \\ \phi_2^d \end{pmatrix} = \begin{pmatrix} \cos\alpha & -\sin\alpha \\ \sin\alpha & \cos\alpha \end{pmatrix} \begin{pmatrix} \psi_1^a \\ \psi_2^a \end{pmatrix}, \quad (1)$$

where α is the mixing angle, which is a function of the nuclear coordinates. ϕ_i^d are no longer eigenstates of the electronic Hamiltonian, but the matrix elements of diabatic energies can be expressed as

$$V_{11}^d = E_1^a \cos^2\alpha + E_2^a \sin^2\alpha, \quad (2)$$

$$V_{22}^d = E_1^a \sin^2\alpha + E_2^a \cos^2\alpha, \quad (3)$$

$$V_{12}^d = V_{21}^d = (E_2^a - E_1^a)\cos\alpha \sin\alpha, \quad (4)$$

in which E_1^a and E_2^a are the adiabatic energies of $1^2A'$ state and $2^2A'$ state, V_{11}^d and V_{22}^d are the diabatic potential energies, and V_{12}^d and V_{21}^d are the coupling potential energies between the two states. By comparison, using the dipole moment operators to obtain the mixing angles is the best choice for the BeH_2^+ system. According to eqn (1), the matrix elements $\langle\psi_3^a|\hat{P}|\psi_1^a\rangle$ and $\langle\psi_3^a|\hat{P}|\psi_2^a\rangle$ can be calculated as

$$\langle\psi_3^a|\hat{P}|\psi_1^a\rangle = \langle\psi_3^a|\hat{P}|\phi_1^d\rangle \cos\langle\alpha + \psi_3^a|\hat{P}|\phi_2^d\rangle \sin\alpha, \quad (5)$$

$$\langle\psi_3^a|\hat{P}|\psi_2^a\rangle = \langle -\psi_3^a|\hat{P}|\phi_1^d\rangle \sin\langle\alpha + \psi_3^a|\hat{P}|\phi_2^d\rangle \cos\alpha, \quad (6)$$

ψ_3^a is the adiabatic state $1^2A''$, which does not involve in the electronic mixing. $\hat{P}$ is the dipole moment operator, which is parallel to the molecular axis for collinear HBe^+H. A simple manner is to make $\langle\psi_3^a|\hat{P}|\phi_1^d\rangle = 0$ and $\langle\psi_3^a|\hat{P}|\phi_2^d\rangle = 1$ for all geometries, so the mixing angle α can be approximated as

$$\alpha = \arctan\left[\left|\frac{\langle\psi_3^a|\hat{P}|\psi_1^a\rangle}{\langle\psi_3^a|\hat{P}|\psi_2^a\rangle}\right|\right]. \quad (7)$$

2.2 *Ab initio* calculations

The single-point energies of the adiabatic states $1^2A'$ and $2^2A'$ and the dipole moments used for diabatic transformation are carried out at the internally contracted multi-reference configuration interaction (MRCI)[37,38] level with a complete active space self-consistent field (CASSCF)[39,40] reference wave function, and the Davidson correction (+Q) is used to compensate for the effect of higher-order correlation. Three states (1A′, 2A′ and 1A″) of BeH_2^+ are equal weight in the state-averaged CASSCF calculations, and 3 valence electrons are included in 16 active orbitals (12a′ + 4a″). The augmented correlation-consistent polarization valence quadruple (AVQZ) basis set is adopted for H and Be atoms. A great range of configuration space is employed so that the PESs are suitable for dynamics calculations at low collision energies, and all *ab initio* points are chosen in the Jacobi coordinates. For the BeH_2^+ system, the Be^+–HH region is defined as $0.6 \le r_{HH}/a_0 \le 18.2$, $0 \le R_{Be^+-HH}/a_0 \le 45$, $0 \le \theta/\text{degree} \le 90$, and the H–$BeH^+$ region is defined as $2.0 \le r_{BeH^+}/a_0 \le 18.2$, $0 \le R_{H-BeH^+}/a_0 \le 45$, $0 \le \theta/\text{degree} \le 180$. To improve the accuracy of fitting PESs, the interaction region has denser energy points distribution than the asymptotic region, and the discontinuous energy points are eliminated. Finally, 33 778 conformations in the coordinate space defined above are selected to generate the diabatic energies. In this work, all of the *ab initio* calculations are performed by MOLPRO program package.[41]

2.3 Fitting the diabatic PESs

Various approaches of constructing PESs, such as many-body expansion method[42–44] and interpolation method,[45,46] have been widely applied. Recent attention has been focused on some more efficient methods based on machine learning to represent global PESs. For example, the NN model[47] is considered as an excellent tool with flexible and accurate

Table 1 Stationary points of the ground state ($1^2A'$) BeH_2^+

	r_{HH} (Bohr)	R_{Be^+-HH} (Bohr)	E (eV)
Equilibrium structure, $\theta = 90°$			
This work[a]	1.450	3.397	−0.384
Artiukhin PES[b]	1.451	3.356	−0.392
MRCI + Q[b]	1.450	3.390	−0.375
CCSD(T)[c]	1.450	3.354	−0.391
CCSDT[c]	1.451	3.356	−0.393
Saddle point, $\theta = 0°$			
This work[a]	1.442	4.146	−0.149
Artiukhin PES[b]	1.438	4.068	−0.150
MRCI + Q[b]	1.440	4.108	−0.147

[a] The adiabatic data E_1^a are obtained by diagonalizing the diabatic matrices in this work. [b] Form ref. 23. [c] Form ref. 56. Energies are relative to the $Be^+ + H_2$ dissociation limit.

Table 2 Spectroscopic constants of $H_2(X^1\Sigma_g^+)$ and $BeH^+(X^1\Sigma^+)$

		This work	Experiment
$H_2(X^1\Sigma_g^+)$	R_e (Bohr)	1.400	1.401
	D_e (eV)	4.732	4.747
	ω_e (cm^{-1})	4400.9	4401.2
	$\omega_e x_e$ (cm^{-1})	127.70	121.33
$BeH^+(X^1\Sigma^+)$	R_e (Bohr)	2.489	2.480
	D_e (eV)	3.160	3.140
	ω_e (cm^{-1})	2205.6	2221.7
	$\omega_e x_e$ (cm^{-1})	37.20	39.79

characteristics for fitting PESs, and it has been used to several reaction systems[48–52] in our previous studies. In this work, the diabatic energies are fitted in analytical forms by the NN method, which are obtained from the transformation of *ab initio* energies using the diabatization method mentioned above. The permutation invariant polynomials (PIP)[53,54] are employed for solving the problem of adaptation of permutation symmetry resulted from the two H atoms for the BeH_2^+ system. A set of functions of internuclear distances are used in the PIP-NN method, which can be written as

$$P_{ij} = \exp(-0.2R_{ij}),\ (i, j = Be^+, H_a, H_b), \tag{8}$$

where R_{ij} and P_{ij} are the distances between the ith and jth atoms and the corresponding monomials, and then the PIP can be represent as

$$G_1 = \frac{1}{2}\left(P_{BeH_a^+} + P_{BeH_b^+}\right), \tag{9}$$

$$G_2 = (P_{BeH_a^+} \times P_{BeH_b^+}), \tag{10}$$

$$G_3 = P_{H_aH_b}. \tag{11}$$

The G_1, G_2, G_3 are normalized treatment as the input data of NN, which written as

$$I_k = \frac{2(G_k - G_{k,\min})}{(G_{k,\max} - G_{k,\min})} - 1, \quad (k = 1, 2, 3), \tag{12}$$

where $G_{i,min}$ and $G_{i,max}$ are the minimum and maximum values of G_i. The neuron is the basic unit of neural network. The output signal y^n of a neuron in the nth layer can be presented as

$$y^n = f^n\left(\sum_{m=1}^{N} w_m{}^n y_m{}^{n-1} + b_m{}^n\right), \tag{13}$$

where N is the number of neurons in the $(n-1)$th layer, f^n is the transfer function, ω_m^n are the connection weights and b_m^n are the biases. The transfer function used in the output layer is linear, whereas the hyperbolic tangent function as the transfer function is used in the hidden layers, written as

$$f(x) = \frac{e^x - e^{-x}}{e^x + e^{-x}}. \tag{14}$$

The NN consists of one input layer, which corresponds to the molecular geometries after PIP processing, one output layer that represents energy and two hidden layers of interconnecting neurons. In this work, the Levenberg–Marquardt algorithm[55] is

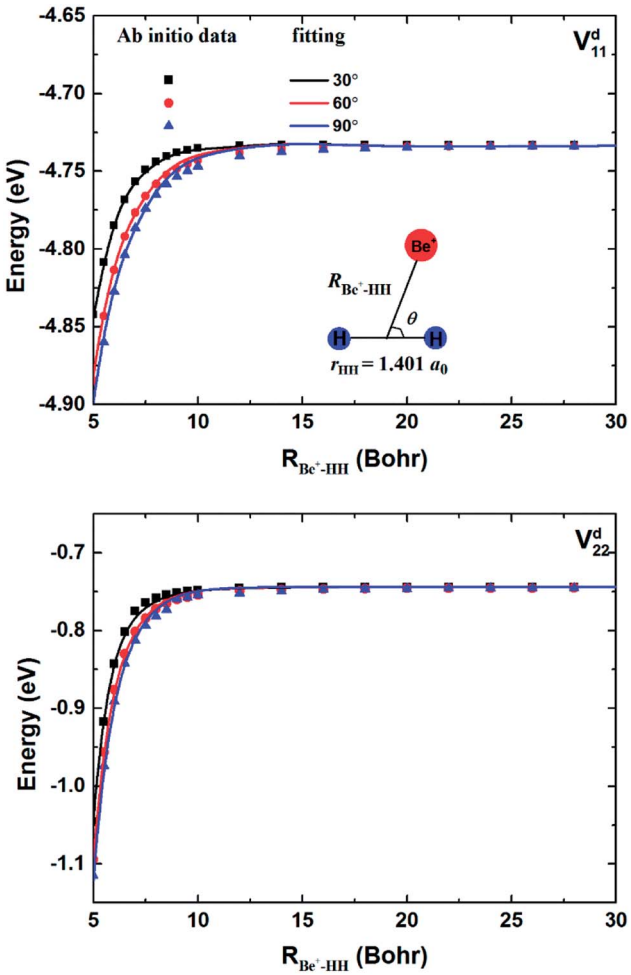

Fig. 1 Comparison of *ab initio* data and fitting results in a long range of the reactant channel as function of R_{Be^+-HH} at $\theta = 30.0°$, 60.0° and 90.0° for fixed $r_{HH} = 1.401a_0$.

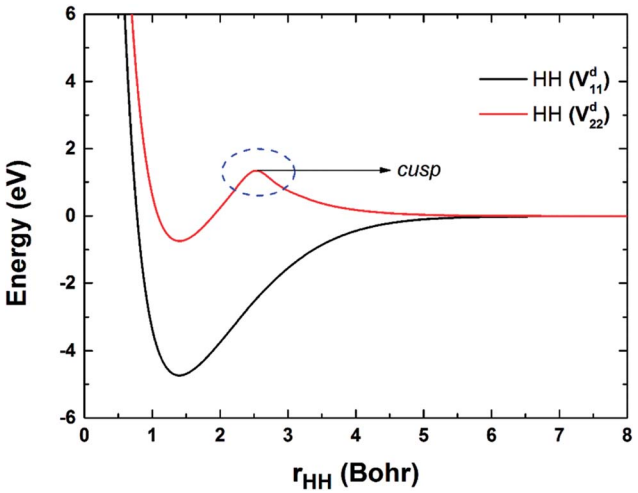

Fig. 2 Potential energy curves of HH obtained on the V_{11}^d and V_{22}^d surfaces.

applied to optimize the connection weights and biases in the process of fitting. An early stopping and the cross validation are employed to avoid the overfitting of NN. The diabatic data are randomly divided into three sets: training set (90 percent), testing set (5 percent), and validation set (5 percent). The training set is used to train the parameters of NN; the testing set is used to test the generalization ability of the training model and the validation set is used to monitor the performance of fitting. The training should be stopped when the validation set error increases, which usually means the appearance of over-fitting. In the training process, 13–14 neurons are included in each hidden layer to fit the diabatic matrix elements. The fitting root mean square errors (RMSEs) for V_{11}^d, V_{22}^d and V_{12}^d, (V_{21}^d) terms are 0.0101, 0.0130 and 0.0132 eV, respectively.

2.4 Features of the diabatic PESs

The geometries and energies of stationary points on the ground state of the Be^+–H_2 complexes are listed in Table 1, compared with the previous studies.[23,56] In this work, the adiabatic data E_1^a are constructed by diagonalizing the matrices $\begin{pmatrix} V_{11}^d & V_{12}^d \\ V_{21}^d & V_{22}^d \end{pmatrix}$, which are obtained by scanning the three diabatic PESs. The values of energy are relative to the $Be^+ + H_2$ dissociation limit. As can be seen, our calculations for the stationary points are good in agreement with Artiukhin PES and the accurate *ab initio* calculations, especially equilibrium structure. The diabatic PESs can reproduce the adiabatic energies well, supporting the fitting results for the V_{11}^d, V_{22}^d and V_{12}^d, (V_{21}^d) matrix elements are accurate enough, and the diabatization method used in this work is reliable for the BeH_2^+ system. Table 2 shows the spectroscopic constants of $H_2(X^1\Sigma_g^+)$ and $BeH^+(X^1\Sigma^+)$ obtained on the diabatic PESs, as compared with the experimental data.[57] The approach is to keep the third atom away from the diatomics

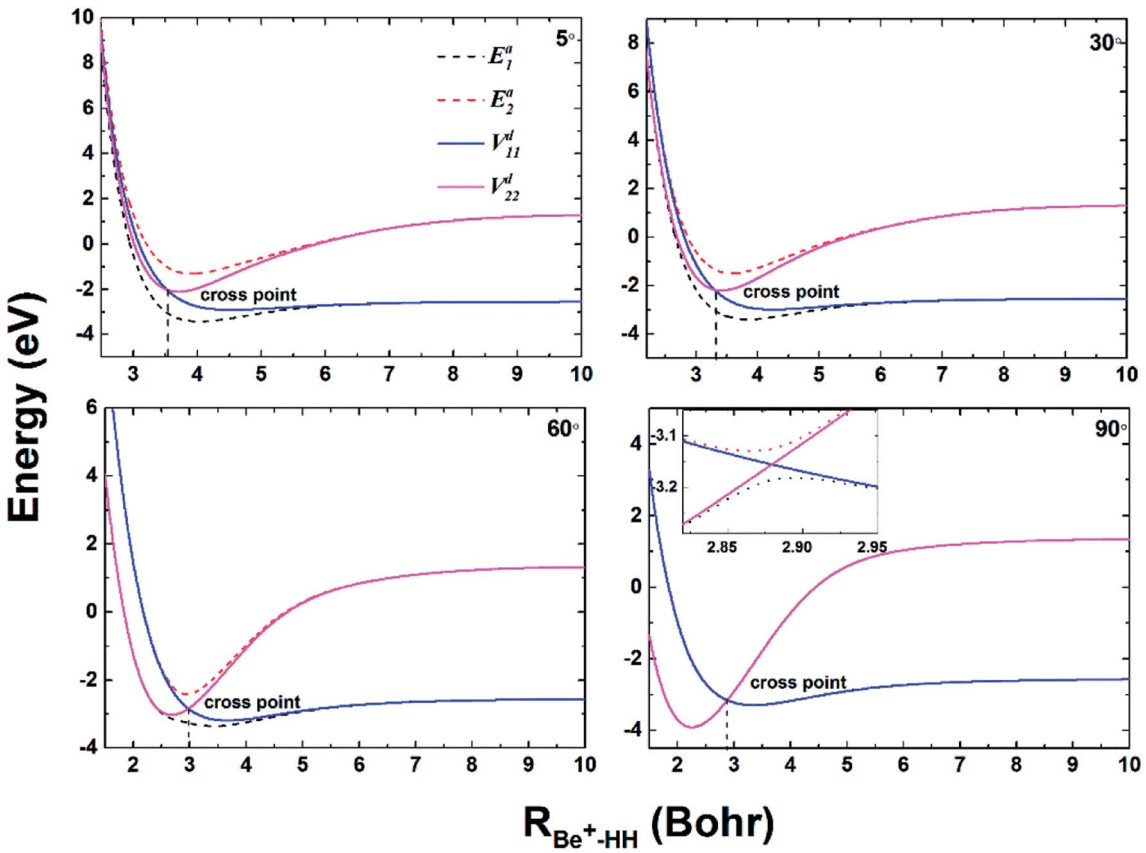

Fig. 3 Adiabatic and diabatic potential energies as function of R_{Be^+-HH} at $\theta = 5.0°$, 30.0°, 60.0° and 90.0° for fixed $r_{HH} = 2.5a_0$.

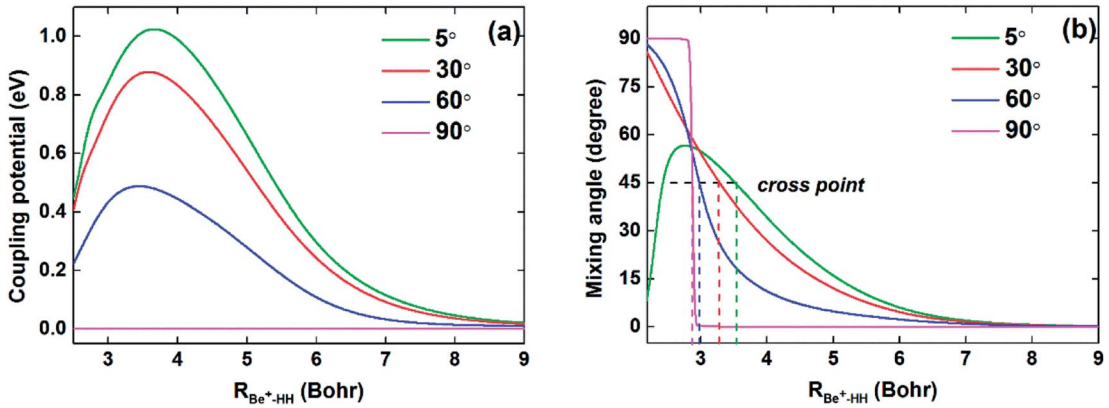

Fig. 4 (a) Coupling potentials and (b) mixing angles as function of R_{Be^+-HH} at $\theta = 5.0°$, 30.0°, 60.0° and 90.0° for fixed $r_{HH} = 2.5a_0$.

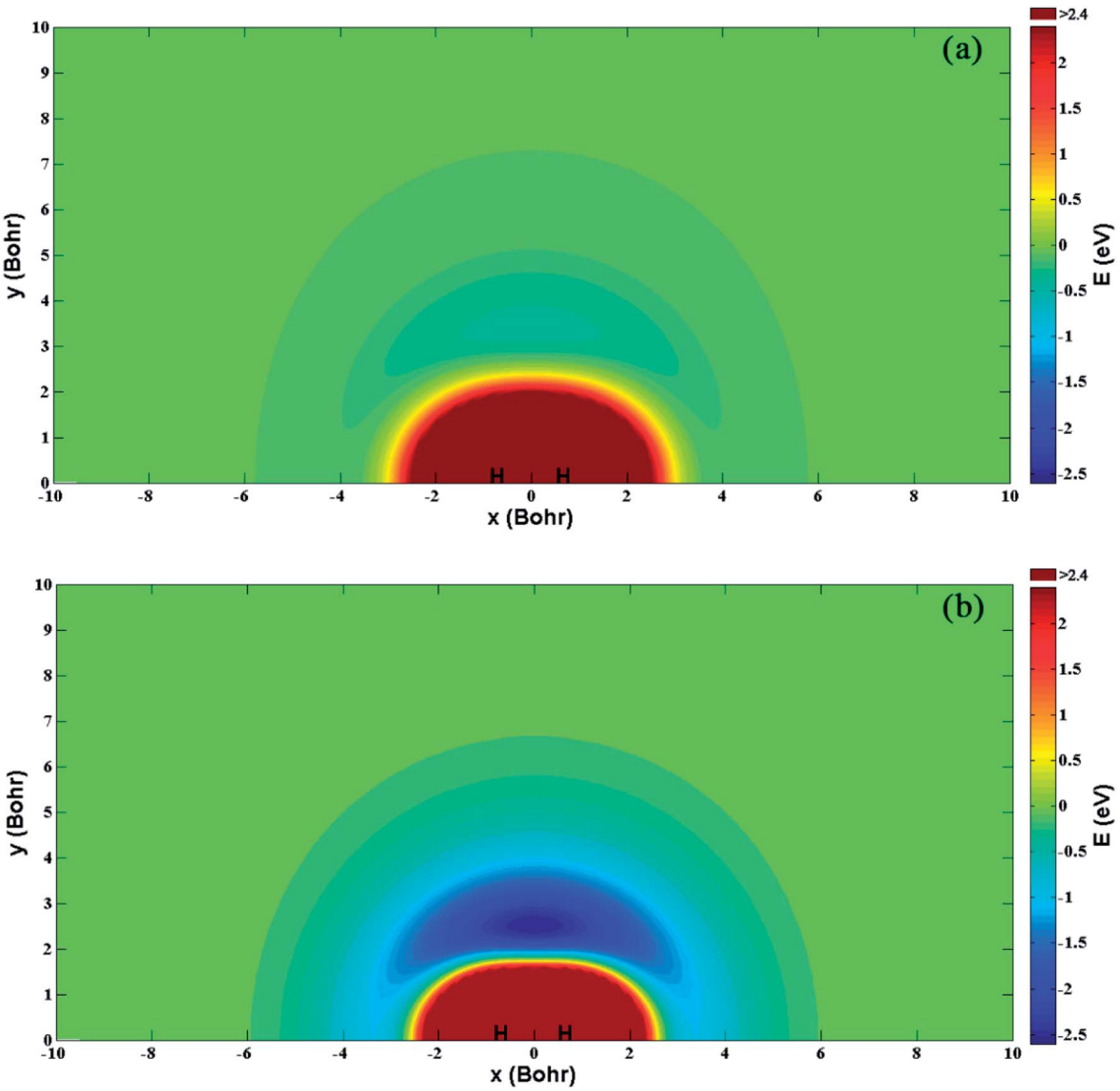

Fig. 5 Color plots of the potential energy when a Be^+ ion moves around the H_2 molecule with the bond length fixed at $1.401a_0$ of the diabatic states (a) V_{11}^d and (b) V_{22}^d.

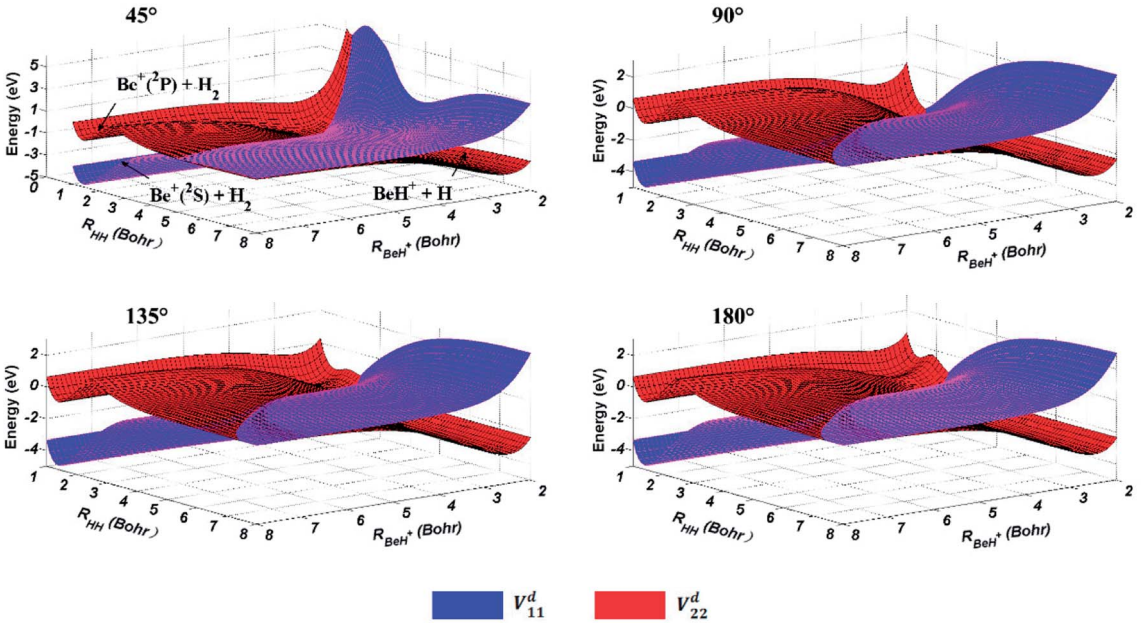

Fig. 6 Potential energy surfaces of the diabatic states V_{11}^d and V_{22}^d for Be^+–H–H angles at 45°, 90°, 135° and 180°.

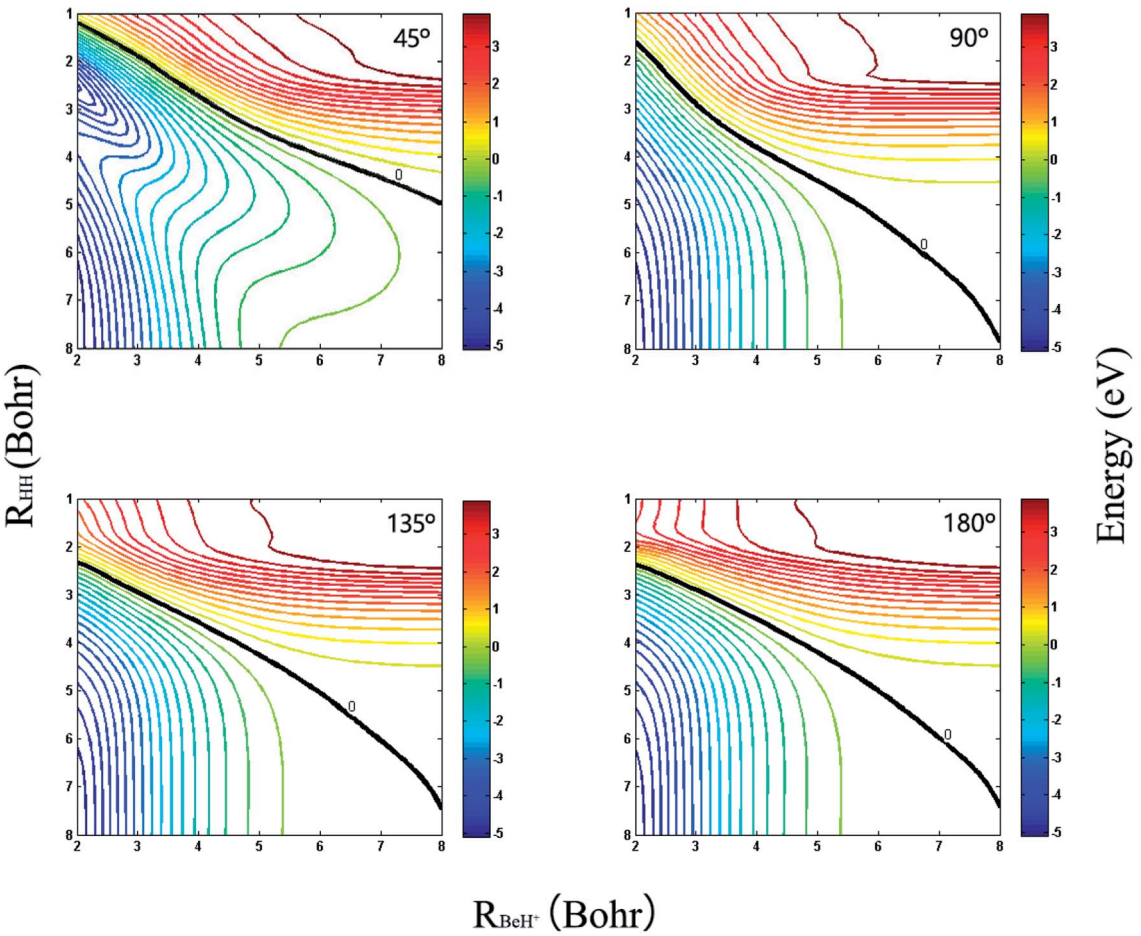

Fig. 7 Contour plots of the ($V_{22}^d - V_{11}^d$) for Be^+–H–H angles at 45°, 90°, 135° and 180°. The black lines represent the positions of intersection.

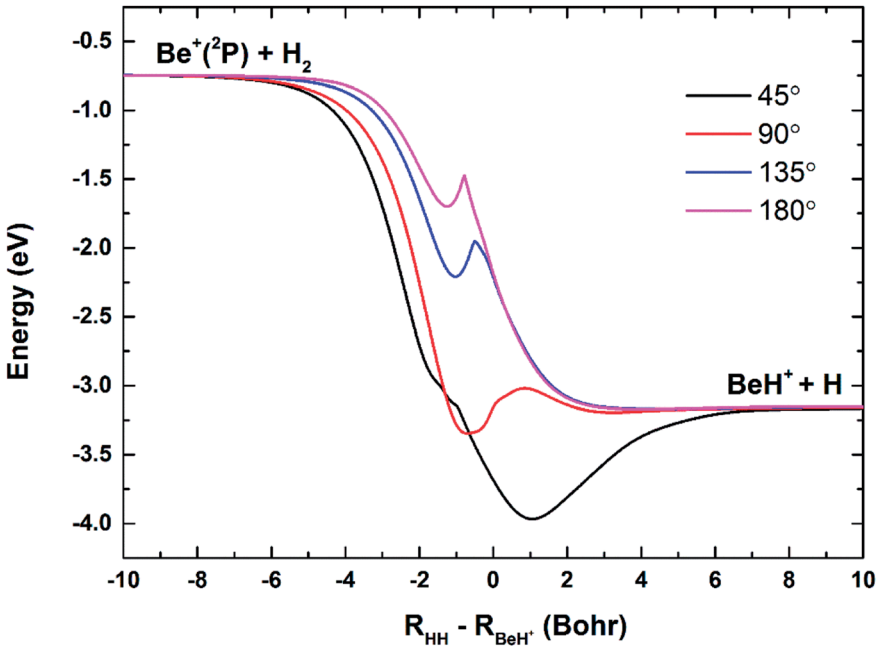

Fig. 8 Minimum energy paths of the diabatic PES V_{22}^{d} for Be^{+}–H–H angles at 45°, 90°, 135° and 180°.

and then to fit the two-body potential curve. The calculated results of bond length, dissociation energy, vibrational frequencies and anharmonicity constants are coincident with the experimental values, indicating the diabatic PESs could describe the two-body potential energies well. In addition, the long-range potential is crucial for ion-neutral reactions, especially at low reaction temperatures. Fig. 1 presents the potential energy values on the V_{11}^{d} and V_{22}^{d} surfaces and corresponding *ab initio* data as function of $R_{Be^{+}–HH}$ for three different θ in a long range of the reactant channel. The r_{HH} is fixed at equilibrium distance. It can be seen that the fitting results are good in agreement with the *ab initio* calculations, implying the NN PESs are reliable for describing the long-range potential.

Fig. 2 shows the potential energy curves of H_2 on the V_{11}^{d} and V_{22}^{d} surfaces, which are obtained by taking points on the diabatic surfaces when the $R_{Be^{+}–HH}$ is set as $50a_0$. The electronic coupling is zero when the Be^{+} is far from H_2, thus the diabatic and adiabatic states are same. On the V_{22}^{d} surface, there exists a cusp on the potential energy curve of two H atoms, which goes against the fitting. The cusp may be attributed to the intersection of higher state, and the intersection states corresponding to $3^2A'$ and $2^2A'$ electronic states in the adiabatic representation.

To compare the potential energies in the adiabatic and diabatic representations clearly, Fig. 3 shows an example of the adiabatic and diabatic potential curves near the entrance channel of the title reaction along $R_{Be^{+}–HH}$ for different four angles θ. The internuclear distance of HH is fixed at $2.5a_0$, which is within the reaction region and could reflect the intersection between the V_{11}^{d} and V_{22}^{d} well. The diabatic potentials are obtained by scanning the diabatic PESs directly and the adiabatic potentials are obtained by diagonalizing the diabatic matrices. The adiabatic potentials avoid each other near the crossing, whereas the diabatic potentials mix and eventually cross over each other. As the increase of θ, the cross point moves to smaller $R_{Be^{+}–HH}$, and the difference between two adiabatic potential curves decreases near the cross point. Moreover, for all cases, the adiabatic and diabatic potential curves are overlapping at large $R_{Be^{+}–HH}$, implying the two states are non-

Table 3 Numerical parameters used in the TDWP calculations

$Be^{+}(^2P) + H_2(X^1\Sigma_g^{+}) \rightarrow BeH^{+}(X^1\Sigma^{+}) + H(^2S)$	
Grid/basis range and size	R (Bohr) $\in [0.01, 22.0]$, $N_R = 219$ r (Bohr) $\in [0.5, 16.0]$, $N_r = 159$ $N_j = 139$
Initial wave packet, $\exp\left[-\frac{(R-R_c)^2}{2\Delta_R^2}\right]\cos k_0 R$	$R_c = 16.5$ Bohr $\Delta_R = 0.20$ Bohr $k_0 = (2E_0\mu_R)^{1/2}$ with $E_0 = 0.50$ eV
Total propagation time	750 000 a.u.
Time steps	15 a.u.
Highest J value	65

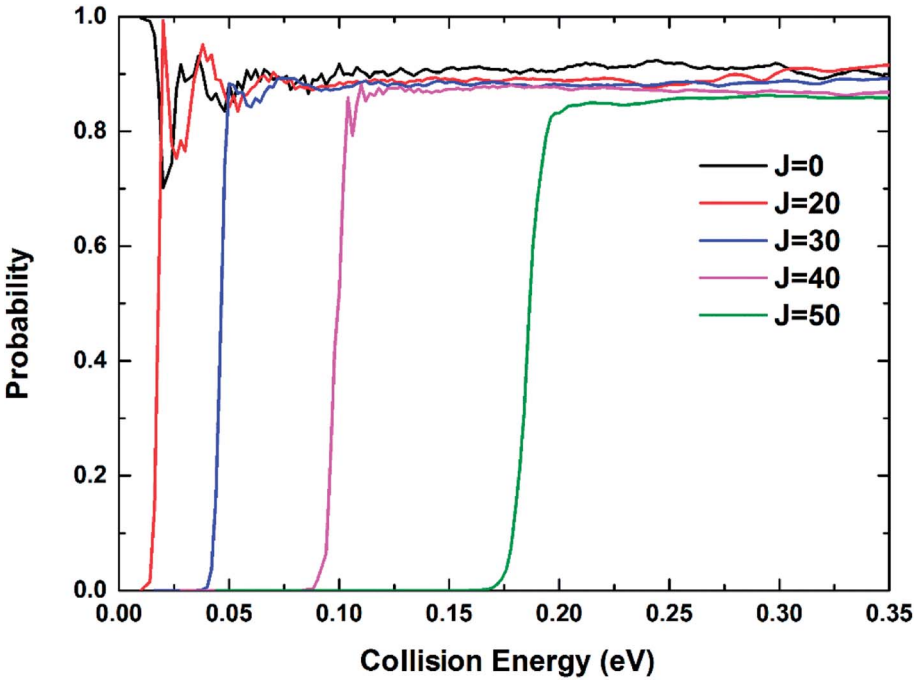

Fig. 9 Total reaction probabilities of the $Be^+(^2P) + H_2(X^1\Sigma_g^+) \rightarrow BeH^+(X^1\Sigma^+) + H(^2S)$ reaction calculated by the TDWP method at $J = 0$, 20, 30, 40 and 50.

degenerate in the long-range region. Fig. 4(a) and (b) give the corresponding coupling potentials and mixing angles shown in Fig. 3, respectively. Fig. 4(a) shows the value of coupling potential declines rapidly with θ increases and gradually decreases to zero when R_{Be^+-HH} value is large enough. It can be explained from eqn (4): as the difference between two adiabatic potential energies increases, the value of coupling potential becomes large. Fig. 4(b) shows the cross point corresponds to the mixing angle of 45°. This conclusion can be obtained from eqn (2) and (3).

Fig. 5(a) and (b) show the energy for a Be^+ moving around a H_2 molecule on the diabatic PESs V_{11}^d and V_{22}^d, respectively. Two H atoms are symmetrically placed on the x-axis and the bond length is fixed at the equilibrium distance ($1.401a_0$) of the ground state. The energy is set as zero when the Be^+ ion is far from the H_2 molecule. There is no obvious barrier or well on the V_{11}^d PES, and the Be^+ ion always feels the repulsive force of the H_2 molecule. For the V_{22}^d PES, there exists a 2.48 eV deep well at $x = 0.0a_0$ and $y = 2.49a_0$, which implies the importance of insertion collision on the V_{22}^d PES. The deep well can attract the Be^+ ion to form the metastable complex Be^+–H_2 and eventually dissociate to the $BeH^+ + H$ products.

The three-dimensional diabatic PESs V_{11}^d and V_{22}^d at four different Be^+–H–H angles (45°, 90°, 135° and 180°) are presented in Fig. 6. The PESs vary smoothly over the coordinate range. For the V_{11}^d PES, only a valley at the left that corresponds to the $Be^+(^2S) + H_2(X^1\Sigma_g^+)$ channel can be found, and there is no valley in the product region, which indicates the fact that the BeH^+ is unstable on the V_{11}^d surface. For the V_{22}^d PES, there exist two valleys at the left and right, which correspond to the $Be^+(^2P) + H_2(X^1\Sigma_g^+)$ channel and the $BeH^+(X^1\Sigma^+) + H(^2S)$ channel, respectively. The $Be^+(^2P) + H_2(X^1\Sigma_g^+) \rightarrow BeH^+(X^1\Sigma^+) + H(^2S)$ reaction starts from the lowest excited state and end at the ground state, and the reactant and product channels are both on the V_{22}^d PES. Moreover, it is evident that the right valley is much lower than the left valley on the V_{22}^d PES, implying the title reaction has the large exothermicity. In order to describe the region of diabatic transition more clearly, the corresponding contour plots for the difference of $(V_{22}^d - V_{11}^d)$ are displayed in Fig. 7, and the exact positions of conical intersection between the V_{11}^d and V_{22}^d are given in black lines. Fig. 8 depicts the minimum energy paths from H_2 to BeH^+ at four approaching angles (45°, 90°, 135° and 180°) on the V_{22}^d PES, which are determined by scanning the PES at different coordinates ($R_{HH} - R_{BeH^+}$) to find the minimum values of energy. The exoergicity of the title reaction is about 2.54 eV when the zero point energy of H_2 (0.27 eV) and BeH^+ (0.14 eV) are included. For the Be^+–H–H angle of 45°, there exists a 0.8 eV deep well on the reaction path, which can support a mass of bound and quasi-bound state complexes. For the Be+–H–H angles of 90°, 135° and 180°, there exist barriers on the reaction paths, and the barrier heights are lower than the energy of reactant channel. The characteristic of the minimum energy paths can reflect that there is no threshold in the title reaction.

3 Dynamics calculations

Based on the diabatic PESs of the BeH_2^+ system, the dynamics studies of the $Be^+(^2P) + H_2(X^1\Sigma_g^+) \rightarrow BeH^+(X^1\Sigma^+) + H(^2S)$ reaction are performed by the TDWP method. The TDWP method is applicable to the diabatic dynamics calculations, and more detailed introduction about this method can be found in

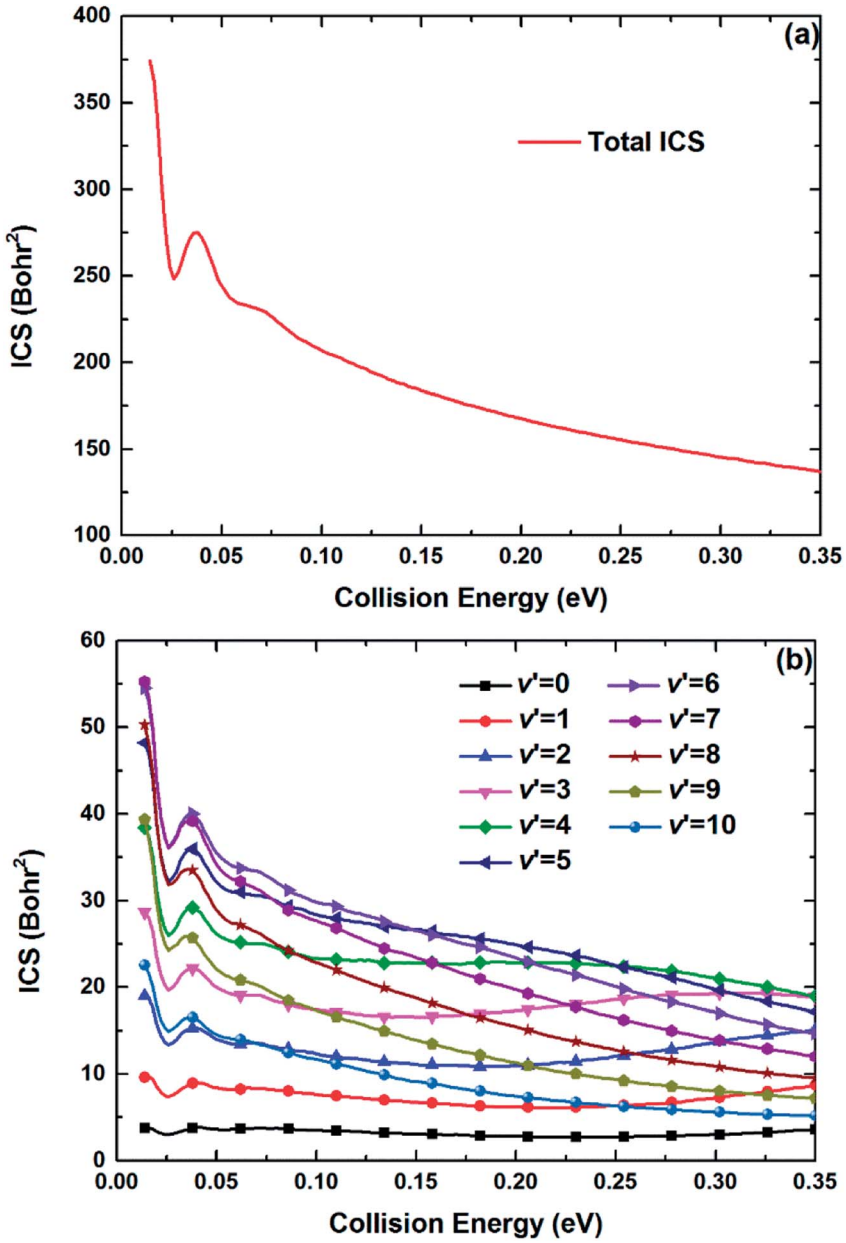

Fig. 10 (a) Total and (b) vibrationally resolved ICSs of the $Be^+(^2P) + H_2(X^1\Sigma_g^+) \rightarrow BeH^+(X^1\Sigma^+) + H(^2S)$ reaction calculated by the TDWP method.

previous literatures.[58,59] In the TDWP calculations, the Coriolis coupling effect is included. Because of the nonadiabatic transition between two states has been considered, so the Hamiltonian is a 2 × 2 matrix, which can be expressed as

$$\hat{H} = -\frac{\hbar^2}{2\mu_R}\frac{\partial^2}{\partial R^2} - \frac{\hbar^2}{2\mu_r}\frac{\partial^2}{\partial r^2} + \frac{\left(\hat{J}-\hat{j}\right)^2}{2\mu_R R^2} + \frac{\hat{j}^2}{2\mu_r r^2} + \hat{V}, \qquad (15)$$

where R and r are the distances of Be^+–H_2 and HH in the Jacobi coordinates, respectively. μ_R and μ_r are the corresponding reduced masses associated with R and r coordinates. $\hat{J}$ and $\hat{j}$ are the angular momentum operators of the BeH_2^+ system and the diatom molecule H_2. $\hat{V}$ is the potential energies, which is a 2 × 2 matrix. The state-to-state S-matrix is extracted by the reactant coordinate based method,[60] and the second-order split operator method is employed in the propagation of wave function. The state-to-state reaction probability is obtained by

$$P_{vj\leftarrow v_0 j_0}{}^{J} = \frac{1}{2j_0+1}\sum_{K,K_0}\left|S_{vjK\leftarrow v_0 j_0 K_0}{}^{J\in}\right|^2. \qquad (16)$$

The state-to-state integral cross sections (ICSs) and differential cross sections (DCSs) are calculated by

$$\sigma_{vj\leftarrow v_0 j_0} = \frac{\pi}{(2j_0+1)k_{v_0 j_0}{}^2}\sum_K\sum_{K_0}\sum_J\left(2J+1\right)\left|S_{vjK\leftarrow v_0 j_0 K_0}{}^{J\in}\right|^2, \qquad (17)$$

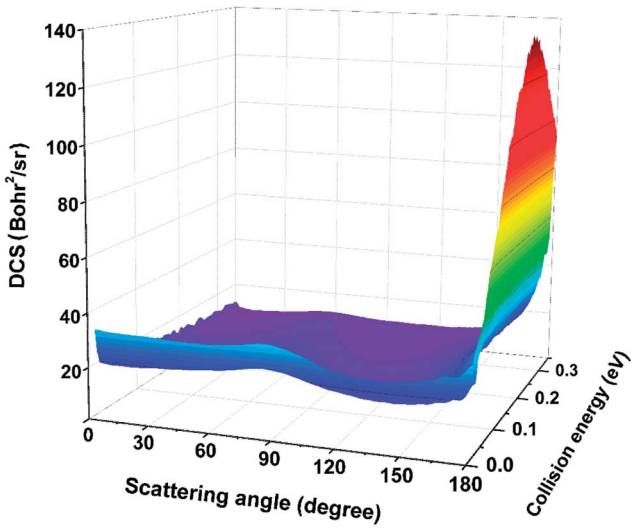

Fig. 11 Three-dimensional plot of the total DCSs for the $Be^+(^2P)$ + $H_2(X^1\Sigma_g^+)$ → $BeH^+(X^1\Sigma^+)$ + $H(^2S)$ reaction calculated by the TDWP method.

and

$$\frac{d\sigma_{vj\leftarrow v_0j_0}(\theta,E)}{d\Omega} = \frac{1}{(2j_0+1)} \times \sum_K \sum_{K_0} \left| \frac{1}{2ik_{v_0j_0}} \sum_J (2J+1) d_{KK_0}{}^J(\theta) S_{vjK\leftarrow v_0j_0K_0}{}^{J\epsilon} \right|^2, \quad (18)$$

where $k_{v_0j_0}$ is the momenta in the entrance channel, θ is the scattering angle and $d_{KK_0}{}^J(\theta)$ is the element of reduced Wigner rotation matrix.

In the TDWP calculations, the initial rovibrational state of the reactant molecule H_2 is chosen as $v_0 = 0$ and $j_0 = 0$. The main parameters used in the TDWP calculations are listed in Table 3.

The reaction probabilities of the $Be^+(^2P)$ + $H_2(X^1\Sigma_g^+)$ → $BeH^+(X^1\Sigma^+)$ + $H(^2S)$ reaction for five different total angular momentum J values (J = 0, 20, 30, 40 and 50) as a function of collision energy are displayed in Fig. 9. For $J = 0$, there is no threshold due to the existence of barrierless reaction path. The threshold appears and gets larger with the increase of J value because of the emergence of centrifugal energy barrier. The dominance of the deep potential well on the V_{22}^d PES leads to some resonance structures in the reaction probability curves, especially at low energies. The oscillations are short-lived and relatively smooth owing to the large exothermicity of the title reaction. The oscillatory amplitude gradually decreases as the collision energy increases, indicating the product escapes the constraint of the potential well more easily.

The maximum of total angular momentum quantum number used in the TDWP calculations is 65, and the corresponding threshold slightly exceeds 0.35 eV, which is set as the upper collision energy limit in the calculations of the ICSs and DCSs. Fig. 10(a) and (b) show the total and several vibrationally resolved (v' = 0–10) ICSs of the title reaction, respectively. Compared with the reaction probability curves, no obvious oscillatory structures can be found on the ICS curves due to the oscillations are erased by summing all the partial waves. The total ICS has a high value, and in general, the total ICS curve represents monotonically decreasing collision energy dependence. This feature can be explained by the V_{22}^d PES. As depicted in Fig. 5(b), the deep well can attract the Be^+ ion when the Be^+ ion moves around the H_2 molecule at a low collision energy, and the system has enough adjustment time to enter the product channel. The adjustment time becomes short when the collision energy increases, thus the ICS value declines. The curves of vibrationally resolved ICSs show an obvious population inversion distribution in the vibrational states of the product BeH^+ molecular ion: the highly excited vibrational states (v' = 6–9) correspond to large ICS values, and the ground vibrational state has the minimum ICS value. This is because the title reaction has the large exothermicity, and the most of energy released from the reactants are transformed into the internal energy of products.

The three-dimensional plot of total DCSs for the $Be^+(^2P)$ + $H_2(X^1\Sigma_g^+)$ → $BeH^+(X^1\Sigma^+)$ + $H(^2S)$ reaction as a function of collision energy is displayed in Fig. 11, which describes the angular distribution of the product BeH^+. As shown in this figure, the angular distribution of BeH^+ is essentially forward–backward symmetric at low collision energy. As the increase of collision energy, the peak at 180° appears, which means the rebound collision becomes obvious for the title reaction. The shapes of DCSs imply the reaction is dominated by a typical direct mechanism, and the product is formed by the short-lived intermediate.

4 Conclusion

This work presents the first global diabatic PESs for the lowest two adiabatic states ($2^2A'$ and $1^2A'$) of the BeH_2^+ system. The scheme to obtain the diabatic energies is based on the dipole moment operators. *Ab initio* energy points are calculated using the MRCI method with the AVQZ basis set. 33 778 geometries in a large region of configuration space are selected to fit the diabatic PESs by using the NN method. The diabatic PESs can reproduce the adiabatic data well and the spectroscopic constants of diatomics calculated on the diabatic PESs are good in agreement with the experimental values. The diabatic PESs topographical features are accounted in detail and the positions of conical intersection between the V_{11}^d and V_{22}^d are pointed. The TDWP calculations for the $Be^+(^2P)$ + $H_2(X^1\Sigma_g^+)$ → $BeH^+(X^1\Sigma^+)$ + $H(^2S)$ reaction are performed on the diabatic PESs. The results of reaction probabilities, ICSs, and DCSs of the title reaction are calculated. The total reaction is no threshold, and there are some oscillatory peaks in the curves of reaction probability. The total ICS has a high value at low collision energy, and the product BeH^+ molecular ion is excited to high vibrational states easily. The DCS results show that the product BeH^+ molecular ion tends to backward scattering at most collision energies.

As we know, no more experimental studies can be obtained to examine our work. We anticipate the present results could stimulate future experiments, and further dynamics researches,

such as the influence isotopic effect or the title reaction under ultracold conditions, can be carried out on the diabatic PESs.

Conflicts of interest

There are no conflicts to declare.

Acknowledgements

This work was supported by the National Natural Science Foundation of China (Grant No. 11774043).

References

1 K. Molhave and M. Drewsen, *Phys. Rev. A*, 2000, **62**, 011401.
2 B. Roth, P. Blythe, H. Wenz, H. Daerr and S. Schiller, *Phys. Rev. A*, 2006, **73**, 042712.
3 P. F. Staanum, K. Hojbjerre, R. Wester and M. Drewsen, *Phys. Rev. Lett.*, 2008, **100**, 243003.
4 N. Kimura, K. Okada, T. Takayanagi, M. Wada, S. Ohtani and H. A. Schuessler, *Phys. Rev. A*, 2011, **83**, 033422.
5 P. Nachtigall, E. Garrone, G. T. Palomino, M. R. Delgado, D. Nachtigallova and C. O. Arean, *Phys. Chem. Chem. Phys.*, 2006, **8**, 2286–2292.
6 M. Felderhoff, C. Weidenthaler, R. von Helmolt and U. Eberle, *Phys. Chem. Chem. Phys.*, 2007, **9**, 2643–2653.
7 M. Dinca and J. R. Long, *Angew. Chem., Int. Ed.*, 2008, **47**, 6766–6779.
8 S. Q. Ma and H. C. Zhou, *Chem. Commun.*, 2010, **46**, 44–53.
9 D. Smith, N. G. Adams, E. Alge and E. Herbst, *Astrophys. J.*, 1983, **272**, 365–368.
10 A. J. Sauval and J. B. Tatum, *Astrophys. J., Suppl. Ser.*, 1984, **56**, 193–209.
11 V. Dryza and E. J. Bieske, *Int. Rev. Phys. Chem.*, 2013, **32**, 559–587.
12 X. G. Zhang and P. B. Armentrout, *J. Chem. Phys.*, 2002, **116**, 5565–5573.
13 C. S. Hinton and P. B. Armentrout, *J. Chem. Phys.*, 2010, **133**, 124370.
14 C. S. Hinton, M. Citir and P. B. Armentrout, *J. Chem. Phys.*, 2011, **135**, 234302.
15 F. X. Li, C. S. Hinton, M. Citir, F. Y. Liu and P. B. Armentrout, *J. Chem. Phys.*, 2011, **134**, 024310.
16 B. C. Sawyer, J. G. Bohnet, J. W. Britton and J. J. Bollinger, *Phys. Rev. A*, 2015, **91**, 011401.
17 P. Blythe, B. Roth, U. Frohlich, H. Wenz and S. Schiller, *Phys. Rev. Lett.*, 2005, **95**, 183002.
18 B. Roth, J. C. J. Koelemeij, H. Daerr and S. Schiller, *Phys. Rev. A*, 2006, **74**, 040501.
19 B. Roth, P. Blythe, H. Daerr, L. Patacchini and S. Schiller, *J. Phys. B: At., Mol. Opt. Phys.*, 2006, **39**, 1241–1258.
20 T. Schneider, B. Roth, H. Duncker, I. Ernsting and S. Schiller, *Nat. Phys.*, 2010, **6**, 275–278.
21 R. D. Poshusta, D. W. Klint and A. Liberles, *J. Chem. Phys.*, 1971, **55**, 252–262.
22 M. Raimondi and J. Gerratt, *J. Chem. Phys.*, 1983, **79**, 4339–4345.
23 D. G. Artiukhin, J. Klos, E. J. Bieske and A. A. Buchachenko, *J. Phys. Chem. A*, 2014, **118**, 6711–6720.
24 R. Abrol and A. Kuppermann, *J. Chem. Phys.*, 2002, **116**, 1035–1062.
25 X. L. Zhu and D. R. Yarkony, *J. Chem. Phys.*, 2010, **132**, 104101.
26 S. Mukherjee, S. Bandyopadhyay, A. K. Paul and S. Adhikari, *J. Phys. Chem. A*, 2013, **117**, 3475–3495.
27 Y. F. Guan, B. N. Fu and D. H. Zhang, *J. Chem. Phys.*, 2017, **147**, 224307.
28 H. J. Werner and W. Meyer, *J. Chem. Phys.*, 1981, **74**, 5802–5807.
29 G. Hirsch, R. J. Buenker and C. Petrongolo, *Mol. Phys.*, 1990, **70**, 835–848.
30 D. R. Yarkony, *J. Phys. Chem. A*, 1998, **102**, 8073–8077.
31 M. Boggio-Pasqua, A. I. Voronin, P. Halvick, J. C. Rayez and A. J. C. Varandas, *Mol. Phys.*, 2000, **98**, 1925–1938.
32 D. He, J. C. Yuan, H. X. Li and M. D. Chen, *Sci. Rep.*, 2016, **6**, 25083.
33 M. H. Alexander, *J. Chem. Phys.*, 1993, **99**, 6014–6026.
34 A. J. Dobbyn and P. J. Knowles, *Mol. Phys.*, 1997, **91**, 1107–1123.
35 A. J. Dobbyn, J. N. L. Connor, N. A. Besley, P. J. Knowles and G. C. Schatz, *Phys. Chem. Chem. Phys.*, 1999, **1**, 957–966.
36 C. Petrongolo, G. Hirsch and R. J. Buenker, *Mol. Phys.*, 1990, **70**, 825–834.
37 H. J. Werner and P. J. Knowles, *J. Chem. Phys.*, 1988, **89**, 5803–5814.
38 P. J. Knowles and H. J. Werner, *Chem. Phys. Lett.*, 1988, **145**, 514–522.
39 H. J. Werner and P. J. Knowles, *J. Chem. Phys.*, 1985, **82**, 5053–5063.
40 P. J. Knowles and H. J. Werner, *Chem. Phys. Lett.*, 1985, **115**, 259–267.
41 H. J. Werner, P. J. Knowles, G. Knizia, F. R. Manby and M. Schutz, *Wires Comput. Mol. Sci.*, 2012, **2**, 242–253.
42 Y. Q. Li, P. Y. Zhang and K. L. Han, *J. Chem. Phys.*, 2015, **142**, 124302.
43 Y. Q. Li, F. C. Ma and M. T. Sun, *J. Chem. Phys.*, 2013, **139**, 154305.
44 L. Guo, H. Y. Ma, L. L. Zhang, Y. Z. Song and Y. Q. Li, *RSC Adv.*, 2018, **8**, 13635–13642.
45 C. X. Xu, D. Q. Xie and D. H. Zhang, *Chin. J. Chem. Phys.*, 2006, **19**, 96–98.
46 M. A. Collins and D. H. Zhang, *J. Chem. Phys.*, 1999, **111**, 9924–9931.
47 H. Rabitz and O. F. Alis, *J. Math. Chem.*, 1999, **25**, 197–233.
48 J. C. Yuan, D. He and M. D. Chen, *Phys. Chem. Chem. Phys.*, 2015, **17**, 11732–11739.
49 J. C. Yuan, D. He and M. D. Chen, *Sci. Rep.*, 2015, **5**, 14594.
50 D. He, J. C. Yuan, H. X. Li and M. D. Chen, *J. Chem. Phys.*, 2016, **145**, 234312.
51 S. F. Wang, J. C. Yuan, H. X. Li and M. D. Chen, *Phys. Chem. Chem. Phys.*, 2017, **19**, 19873–19880.
52 J. C. Yuan, D. He, S. F. Wang, M. D. Chen and K. L. Han, *Phys. Chem. Chem. Phys.*, 2018, **20**, 6638–6647.

53 B. J. Braams and J. M. Bowman, *Int. Rev. Phys. Chem.*, 2009, **28**, 577–606.
54 B. Jiang and H. Guo, *J. Chem. Phys.*, 2013, **139**, 054112.
55 M. T. Hagan and M. B. Menhaj, *IEEE Trans. Neural Netw. Learn. Syst.*, 1994, **5**, 989–993.
56 A. J. Page, D. J. D. Wilson and E. I. von Nagy-Felsobuki, *Phys. Chem. Chem. Phys.*, 2010, **12**, 13788–13797.
57 K. P. Huber and G. Herzberf, *Constants of Diatomic Molecules, Springer*, 1979.
58 Z. G. Sun, S. Y. Lee, H. Guo and D. H. Zhang, *J. Chem. Phys.*, 2009, **130**, 174102.
59 Z. G. Sun, H. Guo and D. H. Zhang, *J. Chem. Phys.*, 2010, **132**, 084112.
60 Z. G. Sun, X. Lin, S. Y. Lee and D. H. Zhang, *J. Phys. Chem. A*, 2009, **113**, 4145–4154.